

DETECTING EXOMOONS AROUND SELF-LUMINOUS GIANT EXOPLANETS THROUGH POLARIZATION

SUJAN SENGUPTA

Indian Institute of Astrophysics, Koramangala 2nd Block, Bangalore 560 034, India; sujan@iiap.res.in

MARK S. MARLEY

NASA Ames Research Center, MS-245-3, Moffett Field, CA 94035, U.S.A.; Mark.S.Marley@NASA.gov

(Received 2016 March 08; Accepted 2016 April 15)

ABSTRACT

Many of the directly imaged self-luminous gas giant exoplanets have been found to have cloudy atmospheres. Scattering of the emergent thermal radiation from these planets by the dust grains in their atmospheres should locally give rise to significant linear polarization of the emitted radiation. However, the observable disk averaged polarization should be zero if the planet is spherically symmetric. Rotation-induced oblateness may yield a net non-zero disk averaged polarization if the planets have sufficiently high spin rotation velocity. On the other hand, when a large natural satellite or exomoon transits a planet with cloudy atmosphere along the line of sight, the asymmetry induced during the transit should give rise to a net non-zero, time resolved linear polarization signal. The peak amplitude of such time dependent polarization may be detectable even for slowly rotating exoplanets. Therefore, we suggest that large exomoons around directly imaged self-luminous exoplanets may be detectable through time resolved imaging polarimetry. Adopting detailed atmospheric models for several values of effective temperature and surface gravity which are appropriate for self-luminous exoplanets, we present the polarization profiles of these objects in the infrared during transit phase and estimate the peak amplitude of polarization that occurs during the the inner contacts of the transit ingress/egress phase. The peak polarization is predicted to range between 0.1 and 0.3 % in the infrared.

Keywords: polarization — scattering — planets and satellites: detection — planets and satellites: atmosphere

1. INTRODUCTION

Natural satellites orbiting all planets except Mercury and Venus are consequential members of the solar system. The formation of a large variety of satellites with size ranging from 2600 km to a few kilometers is a natural consequence of planet formation. Therefore, it seems likely that the abundance of planetary systems discovered around other stars should also have a significant number of natural satellites or exomoons orbiting the planets. Indeed both theoretical investigations on the formation and properties as well as observational searches for exomoons have already been initiated (for a review see [Heller et al. \(2014\)](#)).

Various methods for detecting exomoons have been suggested and almost all of them rely upon photometric light curves of the star during the transit of the planet. For example, barycentric and photocentric Transit Timing Variation (TTV) ([Sartoretti & Schneider 1999](#); [Szabo et al. 2006](#)) and Transit Duration Variation (TDV) ([Kipping 2009](#)) rely upon transit photometry. While TTV is more sensitive to wide-orbit moons, TDV is more sensitive to close-orbit moon. The first and till date the only systematic program searching for exomoons with Kepler (the Hunt for Exomoons with Kepler program) analyzes the transit light curves obtained by Kepler space telescope and attempts to identify the presence of a natural satellite around the transiting planets([Kipping et al. 2012](#)). Unfortunately, the effect of an exomoon on the light curve is so tiny that the expected signature is extremely difficult to identify and therefore, evidence for an exomoon is still elusive.

Apart from transiting planets, another class of giant exoplanets that are young, warm and self luminous have been discovered by direct imaging (e.g., [Chauvin et al. 2004](#); [Marois et al. 2008](#); [Lagrange et al. 2010](#); [Lafrenière et al. 2010](#); [Macintosh et al. 2015](#)). These planets are typically 10-40 AU away from their parent stars. Such a large separation allows them to be spatially resolved with coronagraphic observation as well as differential imaging techniques. In

the next few years, ground-based telescopes with dedicated high-contrast imaging instrumentation, such as the P1640 coronagraph on Palomar, the Gemini Planet Imager on Gemini South, SPHERE on the VLT and James Webb Space Telescope are expected to detect many more such planets (Beichman et al. 2010).

Comparisons of synthetic spectra to observed data clearly implies that most of the exoplanets directly imaged to date have dusty atmospheres (Marois et al. 2008; Lafrenière et al. 2010; Macintosh et al. 2015). In that respect the atmospheres of these planets are very similar to those of L dwarfs. Hence, like the L dwarfs, it is expected that radiation of these planets as well as those likely to be detected in the future, should be linearly polarized in the near-infrared due to scattering by dust grains (Marley & Sengupta 2011). For a homogeneous distribution of scatterers, the net polarization integrated over the projected disk of a spherically symmetric planet is zero. Horizontal inhomogeneity may yield net non-zero polarization (de Kok et al. 2011). On the other hand rotation induced oblateness causes asymmetry and gives rise to significant amount of polarization (Sengupta & Krishan 2001; Sengupta & Marley 2010; Marley & Sengupta 2011). Observed linear polarization of L dwarfs shows that the amount of polarization increases with the increase in spin rotation velocity (Miles-Paez, Zapatero Osorio, Palle & Pena Ramirez 2013). This implies that the asymmetry due to oblateness plays a dominant role. Apart from the asymmetry due to oblateness, net non-zero disk integrated polarization may arise if the stellar disk is occulted by a planet. Several authors have presented detailed models of such transit polarization of stars of different spectral types (Carciofi & Magalhaes 2005; Kostogryz et al. 2011; Wiktorowicz & Laughlin 2014; Kostogryz, Yakobchuk & Berdyugina 2015; Kostogryz & Berdyugina 2015a). Scattering of light in stellar atmosphere gives rise to linear polarization throughout the stellar spectrum. Because of the variation in scattering geometry this polarization increases monotonically from the center of the disk towards the stellar limb. However, since the polarization of hot stars arises because of electron scattering and that for cool stars arises because of Rayleigh scattering of atoms and molecules, the peak amplitude of polarization is extremely small, a few times 10^{-6} in the B-band. On the other hand, as demonstrated by Sengupta & Marley (2010) and Marley & Sengupta (2011), scattering by dust grains yields high polarization in the infrared. In fact the degree of polarization detected from several L dwarfs is as high as 0.1-0.4 % in the I-band for even moderately fast rotating L dwarfs.

In this paper, we suggest that similar to the polarization of a star that arises due to the transit of a planet, the self-luminous directly imaged exoplanets should also give rise to detectable amount of time dependent polarization if the object is eclipsed by a sufficiently large natural satellite or exo-moon. Hence, we propose that exomoons around self-luminous directly imaged planets can be detected through time dependent image polarimetric observation.

In the next section, we briefly describe the atmospheric models adopted. In section 3, we present the formalism used to derive the time dependent eclipse polarization by exomoons of different size and in section 4, we discuss the results. Finally we conclude our investigation in section 5.

2. THE PLANETARY ATMOSPHERIC MODELS AND SCATTERING POLARIZATION

In order to calculate the intensity and polarization of the planetary radiation, we have employed a grid of one-dimensional, hydrostatic, non-gray, radiative-convective equilibrium atmosphere models stratified in plane-parallel. These models incorporate about 2200 gas species, about 1700 solids and liquids for compounds of 83 naturally occurring elements as well as five major condensates as opacity sources (Ackerman & Marley 2001; Marley et al. 2002; Freedman et al. 2008; Saumon & Marley 2008). Silicate and iron clouds computed with sedimentation efficiency $f_{\text{sed}} = 2$ are included in the atmospheric model (Ackerman & Marley 2001). The model atmospheres are calculated for specified values of effective temperature T_{eff} and surface gravities g .

The atmospheric code computes the temperature-pressure profile, the gas and dust opacity and the dust scattering asymmetry function averaged over each atmospheric pressure level. These input data are used in a multiple scattering polarization code that solves the radiative transfer equations in vector form. The two Stokes parameter I and Q are calculated in a locally plane-parallel medium (Sengupta & Marley 2010; Marley & Sengupta 2011). A combined Henyey-Greenstein-Rayleigh phase matrix (Liu & Weng 2006) is used to calculate the angular distribution of the photons before and after scattering. The detailed formalisms as well as the numerical methods for calculating the angle dependent total and polarized intensity I and Q are described in Sengupta & Marley (2009). Finally, the angle dependent I and the polarization $P = Q/I$ computed by the polarization code are integrated over the eclipsed disk of the planet. The formalism is described in the next section. We have neglected thermal and reflected light from the exomoon.

3. ECLIPSED DISK INTEGRATED POLARIZATION

Similar to the case of a transiting planet, the net polarization during eclipse is equal to the fractional circumference blocked by the projection of the moon over the surface of the planet multiplied by the scattering polarization and intensity of the planet at each radial point along the planetary disk.

The disk integrated polarization during the eclipse phase is given by (Carciofi & Magalhaes 2005; Wiktorowicz & Laughlin 2014)

$$p(t) = \frac{1}{F} \int_{r_m(t)-w}^{r_m(t)+w} C(r, t) I(r) P(r) dr, \quad (1)$$

where F is the flux of the unobscured planet, $I(r)$ and $P(r)$ are the specific intensity and polarization respectively at the normalized radial co-ordinate r on the disk of the planet, $w = R_m/R_P$ is the ratio between the radius of the moon (R_m) and the radius of the planet (R_P), $C(r, t)$ is the instantaneous path length along the planetary circumference at r that is eclipsed by the moon and is given as

$$C(r, t) = 2\sqrt{[(r - r_m(t))^2 - w^2]}, \quad (2)$$

$r_m(t)$ being the instantaneous position of the center of the moon and is given by

$$r_m(t) = \left[b^2 + 4 \left\{ (1+w)^2 - b^2 \right\} \left(\frac{t}{\tau} \right)^2 \right]^{1/2}, \quad (3)$$

where $b = a \cos i/R_p$ is the impact parameter for circular orbit of radius a and i is the orbital inclination angle of the moon. In the above expression, t is the time since mid-eclipse and τ is the eclipse duration given by Scharf (2009)

$$\tau = \frac{P}{\pi} \sin^{-1} \left[\frac{R_p}{a} \left\{ \frac{(1+w)^2 - b^2}{1 - \cos^2 i} \right\}^{1/2} \right]. \quad (4)$$

Here, $\mu = \cos \theta$ with θ being the angle between the normal to the planetary surface and the line of sight, $r = \sqrt{1 - \mu^2}$, $0 \leq r \leq 1$. In term of μ , Equation (1), therefore reduces to

$$p(t) = \frac{1}{F} \int_{r_1}^{r_2} 2\sqrt{\frac{[(1 - \mu^2)^{1/2} - r_m(t)]^2 - w^2}{1 - \mu^2}} I(\mu) P(\mu) \mu d\mu, \quad (5)$$

where $r_1 = \sqrt{1 - [r_m(t) + w]^2}$ and $r_2 = \sqrt{1 - [r_m(t) - w]^2}$.

Similar to the orbital period of Ganymede around Jupiter, we have fixed the orbital period of the exomoon at 7 days and have calculated the orbital distance by using Kepler's law. The radius of the planet is fixed at $1R_J$ where R_J is the radius of Jupiter. The mass of the planet is calculated from the surface gravity of the planet. It is worth mentioning that this is just a representative case. The orbital period does not alter the amount of polarization originated due to eclipse but it determines the interval between the two successive amplitudes of polarization that occur at the inner contact points of the transit ingress/egress phase and provides some qualitative guidance to the order of magnitude duration of the polarization event. The polarization profile is calculated for two values of the inclination angle for the satellite, 90° and 88° . Similar to the case of transiting planets, eclipse cannot occur if the inclination angle $i \leq \cos^{-1} \left(\frac{R_p + R_m}{a} \right)$.

4. RESULTS AND DISCUSSION

For transit polarization models of stars, the local angle dependent polarization arises by scattering of light with atoms and molecules and the maximum amount of polarization that occurs at the stellar limb is usually very small. Scattering polarization at different angular or radial points of a solar type star varies from a few times of 10^{-4} near the limb to a few times of 10^{-6} near the center for wavelengths in the range of 4000-5500 Å (Fluri & Stenflo 1999). At longer wavelengths the polarization is much smaller than 10^{-6} . The polarization is of course zero at the center ($\mu = 1$) and maximum at the limb ($\mu = 0$). The contribution of a scattering opacity to the total opacity in the atmosphere is responsible for the center-to-limb variation in the polarization across any stellar disk (Harrington 1969). In hot stars (spectral types O, B or A), electron scattering gives rise to such opacity while Rayleigh scattering by atomic and molecular hydrogen and atomic helium is the main source of scattering opacity in cool stars. The polarization at the limb due to electron scattering is as high as 0.1 (Chandrasekhar 1960) while the polarization for wavelengths of

solar resonant lines such as Ca or Sr, is about 0.16 (Bianda, Stenflo & Solanki 1999). This is about three orders of magnitude higher than the polarization at the solar limb observed in the solar continuum (Fluri & Stenflo 1999). On the other hand, if the planetary radiation is polarized by dust scattering then the amount of polarization at the limb for the far optical and infrared wavelength should be higher than that arises due to electron scattering at near optical wavelength. As realized by Carciofi & Magalhaes (2005), formation of dust grains in the cloudy atmosphere of L brown dwarfs would provide an additional scattering opacity to the gas opacity which should yield into large values for limb polarization. The self-luminous giant exoplanets are also expected to have cloudy atmosphere and linear polarization as large as 1-2% in the infrared is already predicted by Marley & Sengupta (2011).

In order to check the validity of the formalism adopted and the correctness of the numerical calculations, we reproduced the transit polarization profiles presented by Carciofi & Magalhaes (2005). These authors used the analytical expressions for the limb darkening law suggested by Claret (2000) and for the solar continuum polarization suggested by Fluri & Stenflo (1999). Carciofi & Magalhaes (2005) also estimated the maximum transit polarization of a T-dwarf of radius $0.2 R_{\odot}$ occulted by an earth size exoplanet. For $R_m/R_P = 0.046$, Carciofi & Magalhaes (2005) found the peak amplitude of transit polarization at wavelength 4600 \AA is 1.6×10^{-4} or 0.016%. As presented in figure 1, for the same value of R_m/R_P and for a central eclipse ($i=90^\circ$), we find the peak polarization to be 0.02% at the B-band, in good agreement with the result of Carciofi & Magalhaes (2005). Figure 1 presents the eclipse polarization profiles at B-, I-, J- and H-bands of a self-luminous cloudy exoplanet of radius $1R_J$. At B-band, Rayleigh scattering by molecules dominates over dust scattering. As the wavelength increases, dust scattering becomes more important in determining the amount of polarization. Figure 1 shows that the eclipse polarization profiles for B- and I-bands are almost the same but the peak polarization increases by about six times at J-band. That the polarization at J-band is much higher than the polarization at I-band is already demonstrated by Marley & Sengupta (2011) for a variety of atmospheric and cloud models. The polarization however, decreases at H-band as the wavelength of the radiation increases farther. The wavelength dependency of the polarization is governed by the adopted cloud model, e.g., the size distribution, the number density of the dust grains as well as the location of the cloud base and deck.

The disk integrated polarization of a spherical exoplanet eclipsed by an exomoon is presented in figure 2 for two different values of the orbital inclination angles and three different sizes of the exomoon. The disk integrated polarization of a unobscured oblate planet is also presented for comparison. Disk integrated polarization of a rotation-induced non-spherical and eclipsed planet could be complicated owing to the fact that the net polarization depends on the angle between the spin axis of the planet and the orbital plane of the exomoon. Since it is not possible to determine the spin axis orientation of the exoplanet, we restrict our polarization models for slow rotating eclipsing planets for which the departure from sphericity is too small to yield net non-zero polarization when it is not in eclipsing phase. The projected spin angular velocity of a few self-luminous exoplanets has already been derived from observation (Marois et al. 2010; Snellen et al. 2014) which can provide the minimum value of the oblateness of the object. Disk integrated polarization for oblate self-luminous giant exoplanets has been presented by Marley & Sengupta (2011) for various values of the spin period, surface gravity and effective temperature. We have neglected any inhomogeneous distribution of scatters. Our atmospheric models consider vertically inhomogeneous but horizontally homogeneous cloud distributions.

As shown in figure 2, the qualitative feature of the eclipse polarization profile is the same to that of transit polarization presented by Carciofi & Magalhaes (2005); Kostogryz et al. (2011) and Kostogryz, Yakobchuk & Berdyugina (2015). The double peaked polarization profile arises because of the fact that the maximum polarization occurs near the inner contacts of ingress/egress phases. For central eclipse i.e., when the inclination angle $i = 90^\circ$, the projected position of the center of the moon during mid eclipse is at the center of the planet causing a symmetry to the projected stellar disk. Hence the disk integrated polarization for central eclipse is zero during mid eclipse. The polarization increases as the moon moves from the center ($t = 0$) to the limb ($t = \pm\tau/2$) of the planetary disk as it induces asymmetry to the planetary disk. However, when the eclipse is off center, i.e., $i < 90^\circ$, the polarization is non-zero during the whole eclipse epoch. The net polarization at the mid eclipse increases with the decrease in the orbital inclination angle of the moon. However, the peak polarization at the limb remains the same irrespective of the inclination angle. Therefore, the peak polarization is independent on the orbit inclination but depends on the radii ratio of satellite to planet. The transit duration depends on the size of both the moon and the planets, on the orbital distance of the moon from the planet and on the inclination angle. Therefore, for a given orbital distance, the peak polarization occurs at different time for different size ratio and inclination angle. Figure 2 shows that the peak polarization at the inner contacts of the ingress/egress phase increases linearly with the increase in the size of the exomoon. At J-band the maximum degree of linear polarization for $R_m/R_p = 0.046$ is 0.11% while that for $R_m/R_p = 0.07$ and 0.1 are 0.16% and 0.21% respectively. In the absence of an eclipsing exomoon, 0.1% of linear polarization can arise only if the spin-rotation period of the planet with surface gravity $g = 30 \text{ ms}^{-2}$ is less than 6.6 hours while it needs a spin rotation period less

than 6.1 hours to yield net non-zero disk integrated polarization of degree 0.2 %. For higher surface gravity, an even shorter period is required in order to yield sufficient oblateness to the planet. Therefore, the time dependent eclipse polarization can be distinguished from the disk integrated polarization of an oblate planet if the spin rotation period of the planet is higher than 10-15 hours so that the asymmetry due to spin-rotation is negligible.

Marley & Sengupta (2011) and Sengupta & Marley (2010) have demonstrated that the degree of polarization of cloudy self-luminous exoplanets and L dwarfs depends on the effective temperature and the surface gravity of the objects. In figure 3, we present the eclipse polarization profiles for exoplanets with different effective temperature and surface gravity. At the lowest surface gravity $g = 30\text{ms}^{-2}$ among the three cases we consider, the highest polarization is obtained at J-band when $T_{\text{eff}} = 800$ K. If the temperature increases further, the cloud base shifts upward yielding a smaller column of dust grains in the observed atmosphere and hence the polarization decreases with the increase in effective temperature. A balance between the downward transport by sedimentation and upward turbulent diffusion of condensates and gas determines the scattering opacity and hence the polarization for different effective temperature and surface gravity. For $g = 56\text{ms}^{-2}$, the polarization is maximum at $T_{\text{eff}} = 1000$ K and it decreases both with the increase and decrease in effective temperature. In fact figure 3 does not show much difference in polarization for $T_{\text{eff}} = 1200$ and 1000 K. On the other hand, at the highest surface gravity considered here, $g = 100\text{ms}^{-2}$, the polarization is greatest at $T_{\text{eff}} = 1200$ K but decreases at lower effective temperatures. Therefore, a combination of the surface gravity and effective temperature along with the size of the exomoon as compared to the exoplanet determine the amount of polarization caused by the eclipse. However, the difference in the amount of polarization among these cases is likely too small to be differentiated observationally. Moreover, the effect of surface gravity and effective temperature can be realized even without the eclipsing effect. For example, a sufficiently fast rotator that may yield detectable amount of net non-zero polarization would show the same properties of the polarization profile. Finally, as seen from figure 3, if T_{eff} is as low as 600 K then for any surface gravity, the polarization reduces substantially owing to less amount of dust grains in the atmosphere probed in the near-infrared in these models. It is worth mentioning that the orbital separation or the inclination angle does not alter the peak amplitude of polarization but alters the overall polarization profile.

5. CONCLUSIONS

We suggest that time resolved imaging polarimetry may be a potential technique to detect large exomoon around directly imaged self luminous exoplanets. The cloudy atmosphere of such planets ensure high polarization due to scattering by dust grains. However, the disk-integrated net polarization would be zero if the planet is spherically symmetric. This symmetry is broken if either the planet loses sphericity due to fast spin rotation, has horizontally inhomogeneous cloud structures or if a sufficiently large satellite eclipses the planetary surface. Asymmetry by a combination of more than one of the above causes is also possible. Assuming a spherical exoplanet eclipsed by an exomoon, we estimated the peak polarization at the inner contact points of ingress/egress phase and presented the eclipse polarization profile. Our investigation implies that detectable amount of polarization may arise in J-band if the planet is eclipsed by a large exomoon. For a central eclipse, the detectable amount of polarization would arise only at the inner contacts of ingress/egress phase while for off central eclipse, polarization may be detectable during the entire eclipsing phase. Unlike the constant polarization that may be detected for fast rotating exoplanet, no polarization will be detected when the planet is out of the eclipse phase.

According to our estimation, an image polarimeter with sensitivity ranging from 0.3 to 0.01 % may detect the presence of exomoon around the self-luminous exoplanets that are directly imaged. Future high-contrast imaging instruments on thirty-meter class telescopes may plausibly provide both the time resolution and polarimetric sensitivity to detect such moons.

6. ACKNOWLEDGEMENTS

We thank the reviewer for a critical reading of the manuscript and for providing several useful suggestions.

REFERENCES

Ackerman, A. & Marley, M. S. 2001, ApJ, 556, 872.
 Bianda, M., Stenflo, J. O., & Solanki, S. K. 1999, A&A, 350, 1060
 Beichman, C. A., et al. 2010, PASP, 122, 162
 Carciofi, A. C., & Magalhaes, A. M. 2005, ApJ, 635, 570
 Chandrasekhar, S. 1960, Radiative Transfer (New York: Dover)
 Chauvin, G., Lagrange, A.-M., Dumas, C., Zuckerman, B., Mouillet, D., Song, I., Beuzit, J.-L., & Lowrance, P. 2004, A&A, 425, L29
 Claret, A. 2000, A&A, 363, 1081

de Kok, R. J., Stam, D. M., & Karalidi, T. 2011, *ApJ*, 741, 59

Fluri, D. M., & Stenflo, J. O. 1999, *A&A*, 341, 902

Freedman, R. S. et al. 2008, *ApJS*, 174, 71.

Harrington, J. P. 1969, *AstrophysL*, 3, 165

Heller, R., Williams, D., Kipping, D., et al. 2014, *AsBio*, 14, 798

Kostogryz, N. M., Yakobchuk, T. M., Morozhenko, O. V., & VidMachenko, A. P. 2011, *MNRAS*, 415, 695

Kostogryz, N. M., Yakobchuk, T. M., & Berdyugina, S. V. 2015, *ApJ*, 806, 97

Kostogryz, N. M. & Berdyugina, S. V. 2015, *A&A*, 575, 89

Kipping, D. M., Bakos, G. A., Buchhave, L., Nesvorný, D., & Schmitt, A. 2012, *ApJ*, 750, 115

Kipping, D. M. 2009, *MNRAS*, 392, 181

Lafrenière, D., Jayawardhana, R., & van Kerkwijk, M. H. 2010, *ApJ*, 719, 497

Lagrange, A.-M., et al. 2010, *Science*, 329, 57

Liu, Q. & Weng, F. 2006, *Applied Optics*, 45, 7475.

Macintosh, B., Graham, J. R., Barman, T., et al. 2015, *Science*, 350, 64

Marley, M. S. & Sengupta, S. 2011, *MNRAS*, 417, 2874

Marley, M. S. et al. 2002, *ApJ*, 568, 335.

Marois, C., Zuckerman, B., Konopacký, Q. M., Macintosh, B., & Barman, T. 2010, *Nature*, 468, 1080

Marois, C., Macintosh, B., Barman, T., Zuckerman, B., Song, I., Patience, J., Lafrenière, D., & Doyon, R. 2008, *Science*, 322, 5906

Miles-Pez, P. A., Zapatero Osorio, M. R., Pall, E., & Pea Ramrez, K. 2013, *A&A*, 556, 125

Sartoretti, P., & Schneider, J. 1999, *A&AS*, 134, 553

Saumon, D., & Marley, M. S. 2008, *ApJ*, 689, 1327

Scharf, C. A. 2009, *Extrasolar Planets and Astrobiology*, Chapter 9 (University Science Books : Sausalito, California).

Sengupta, S. & Krishan, V. 2001, *ApJ*, 561, L123

Sengupta, S. & Marley, M. S. 2009, *ApJ*, 707, 716

Sengupta, S. & Marley, M. S. 2010, *ApJL*, 722, L142

Snellen, I. A. G., Brandl, B. R., de Kok, R. J., Brogi, M., Birkby, J. & Schwarz, H., 2014, *Nature*, 509, 63

Szabo, G. M., Szatmary, K., Diveki, Z., & Simon, A. 2006, *A&A*, 450, 395

Wiktorowicz, S. J., & Laughlin, G. P. 2014, *ApJ*, 795, 12

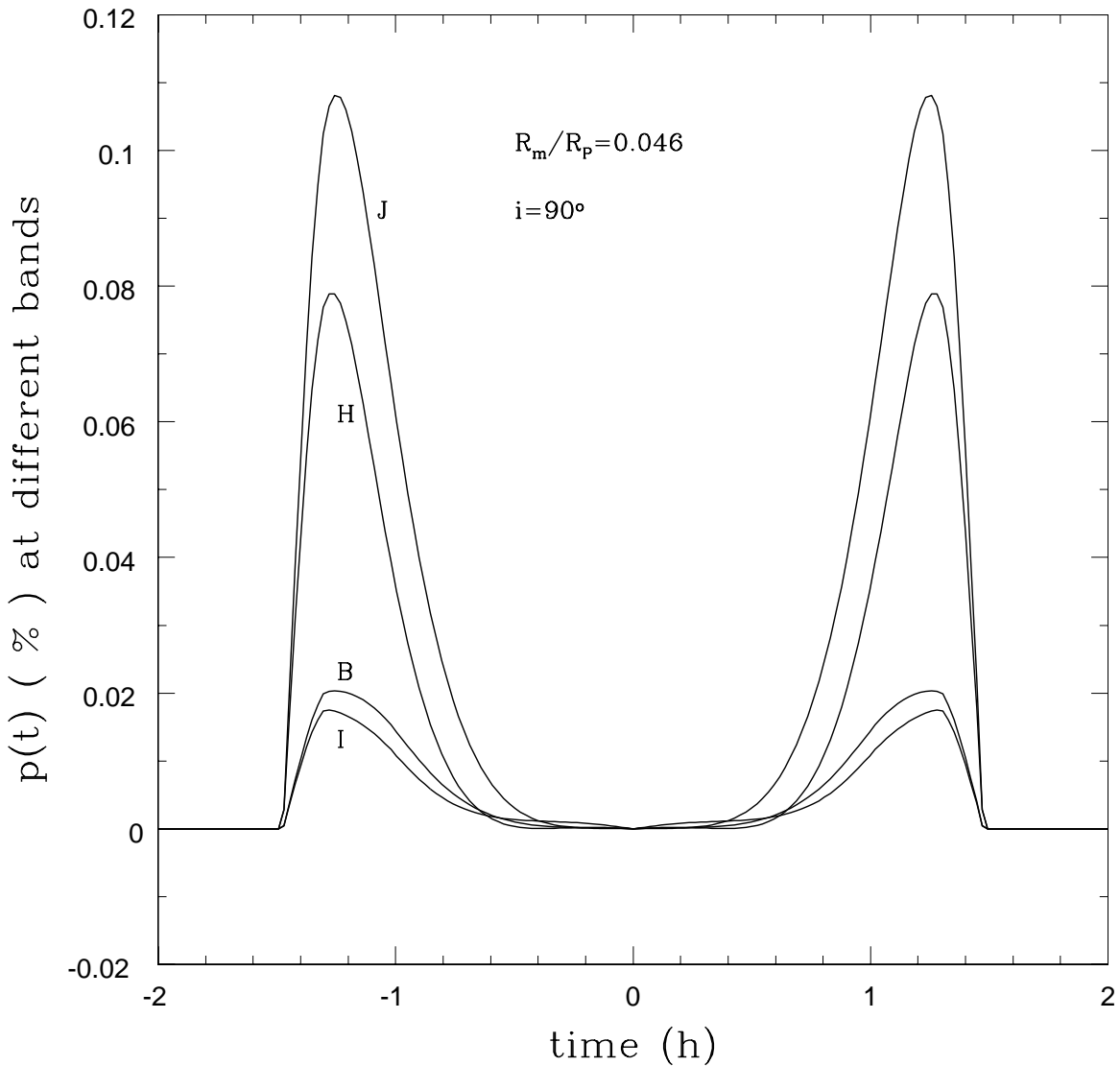


Figure 1. Disk integrated linear polarization at different wavelength bands of a self-luminous spherical exoplanet partially eclipsed by a moon of radius 0.046 times the radius of the planet.

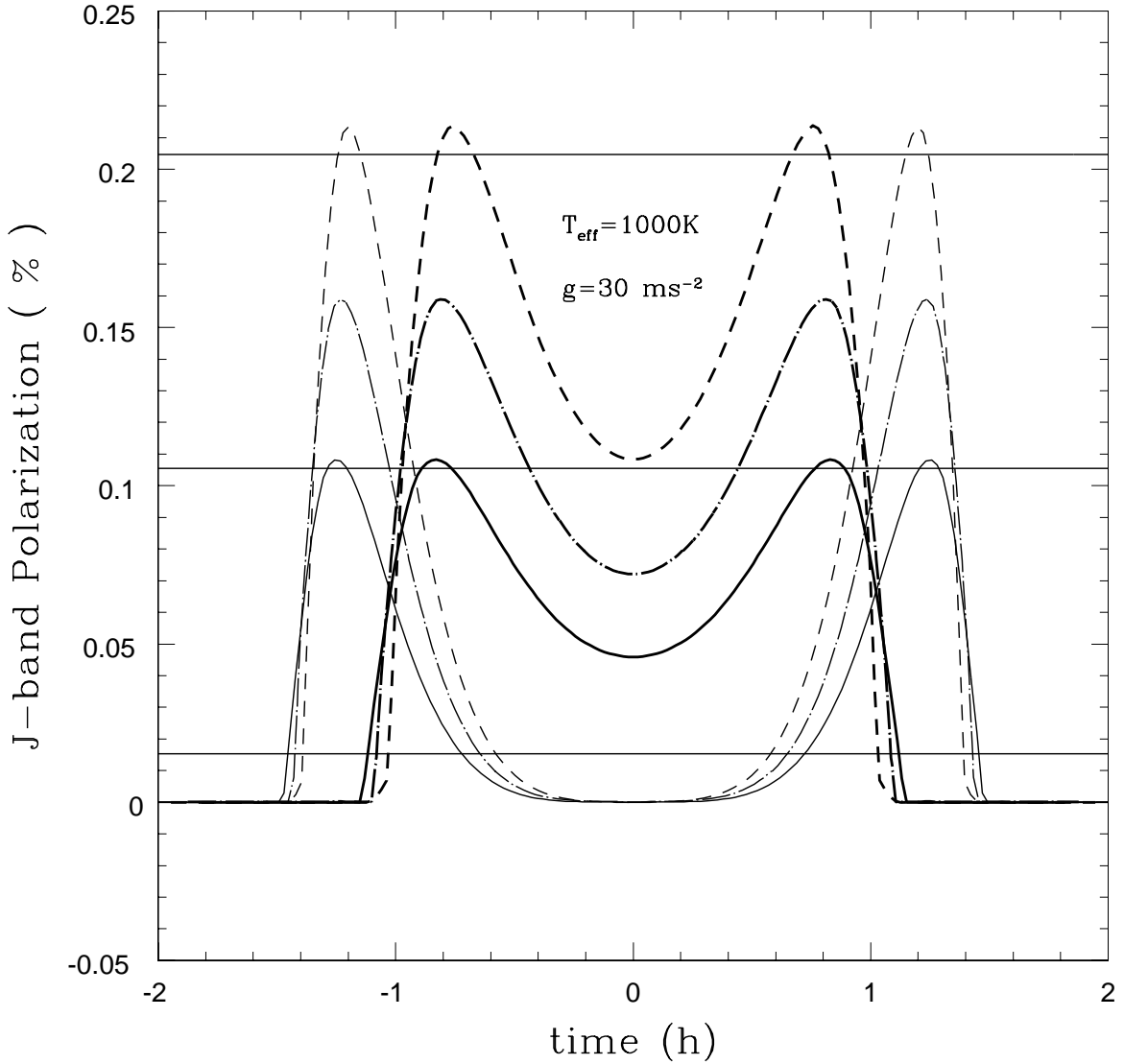


Figure 2. J-band disk integrated polarization of self-luminous, spherical exoplanets partially eclipsed by an exomoon. Thin and thick lines represent the percentage polarization for an exomoon transit with an orbital inclination angle of $i = 90^\circ$ and 88° respectively. Solid lines, dashed-dot lines and dashed lines represents eclipse polarization profile with $R_m/R_P=0.046$, 0.07 and 0.1 repectively. The orbital period of the exomoon is set to 7 days for all cases. From top to bottom, the horizontal lines represent linear polarization integrated over the disk of a rotation-induced oblate exoplanet (with no eclipse) with spin period 6.1, 6.6, and 15 hours respectively.

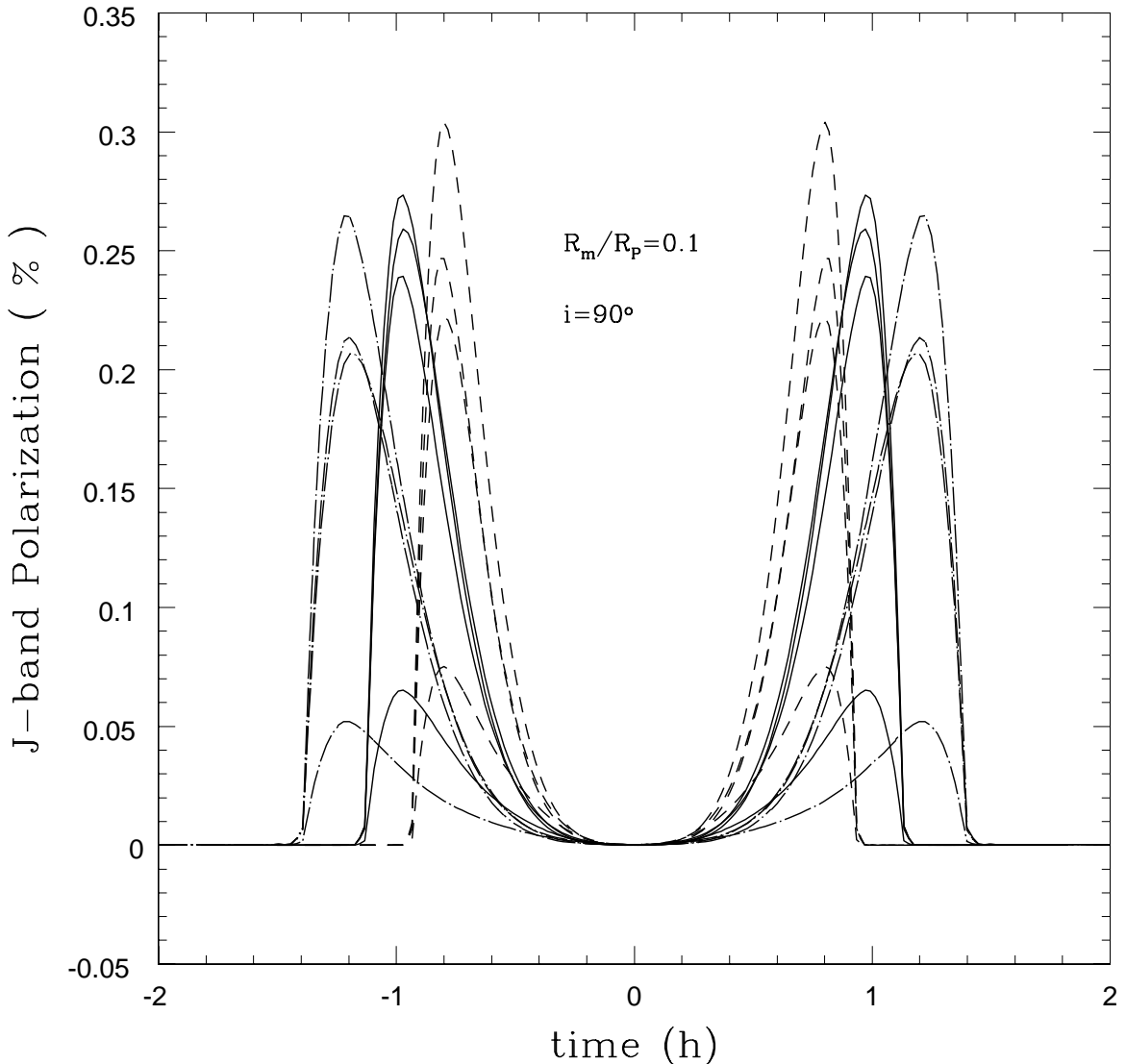


Figure 3. J-band polarization of exoplanets with different effective temperature and surface gravity. Solid lines represent exoplanetary models with $g = 56 \text{ ms}^{-2}$; from top to bottom the solid lines represents models with $T_{eff} = 1000, 1200, 800$ and 600 K . Dashed lines represent the polarization with $g = 100 \text{ ms}^{-2}$ and from top to bottom dashed lines represent models with $T_{eff} = 1200, 1000, 800$ and 600 K . Similarly, dot-dashed line represents model with $g = 30 \text{ ms}^{-2}$ and from top to bottom, the dot-dashed lines represent exoplanet models with $T_{eff} = 800, 1000, 1200$ and 600 K .